CHEMISTRY OF MATERIALS

pubs.acs.org/cm

Article

A-Cation-Dependent Excited State Charge Carrier Dynamics in Vacancy-Ordered Halide Perovskites: Insights from Computational and Machine Learning Models

Pabitra Kumar Nayak, Carlos Mora Perez, Dongyu Liu, Oleg V. Prezhdo, and Dibyajyoti Ghosh*

Cite This: *Chem. Mater.* 2024, 36, 3875−3885

Read Online

ACCESS | Metrics & More | Article Recommendations | Supporting Information

ABSTRACT: Lead-free vacancy-ordered halide perovskites (VOHPs) are emerging as promising materials for environmentally friendly next-generation optoelectronic devices. However, a detailed atomistic understanding of charge carrier dynamics under ambient conditions (300 K) is lacking. Thus, attempts to refine the optoelectronic performance of VOHPs through material selection remain challenging. Here, we combine nonadiabatic molecular dynamics, time-domain density functional theory, and an unsupervised machine learning (ML) model for in-depth analyses of prevailing nonradiative carrier recombination and its entropy correlation with real-time structural dynamics. Our key findings illustrate that the thermal fluctuations are intricately linked to the performance-limiting nonradiative recombination in these perovskites. The detailed ML model-based analyses reveal the complex nonlinear correlations between photophysical properties and several structural features that dominantly influence excited state carrier dynamics. The atomistic insights unambiguously demonstrate that the organic methylammonium (MA) cation as the A cation in the lattice significantly impacts thermal fluctuations of the isolated inorganic metal halide octahedral subsystem. The stronger electron−phonon interactions introduce substantially faster nonradiative carrier relaxation over time. The inorganic elements, cesium and rubidium (A cations), largely restrict the lattice dynamics, weakening instantaneous nonradiative electron−phonon coupling in VOHPs. These inorganic VOHPs exhibit longer carrier lifetimes, depicting suppressed nonradiative carrier recombination processes. Our study emphasizes the decisive impacts of complex dynamic structure−excited state property correlations on the charge carrier dynamics in a group of primarily isostructural halide perovskites. This study provides valuable insights into the strategically designed lead-free perovskites for optoelectronic device applications.

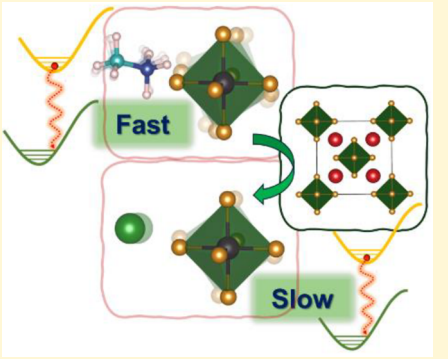

INTRODUCTION

Metal halide perovskites (MHPs) have fascinated the optoelectronics community due to their compositional and structural variety, which result in a wide range of functional applications, including solar cells,[1,2] light-emitting diodes (LEDs),[3,4] photocatalysis,[5,6] and photodetection.[7,8] These materials exhibit attractive properties such as high absorption coefficients, tunable band gaps, defect tolerance, and long carrier diffusion lengths.[9,10] Despite the promising optoelectronic properties of halide perovskites, the toxicity of lead and the long-term material stability have remained the bottlenecks for their commercialization as next-generation optoelectronic devices.[11−14] In this regard, vacancy-ordered halide perovskites (VOHPs) are attracting unprecedented attention due to their structural and chemical stability, compositional diversity, and promising photoactivity.[15−17] The prototype of the VOHP structure, A_2BX_6 [A, monovalent (in)organic cation; B, tetravalent metal cation; X, halide anion], can be constructed by eliminating alternate metal sites of conventional ABX_3 MHPs in all three dimensions. Such structural engineering leads to doubling of the oxidation state of the B-site metal cation, +4, opening new chemical space for finding potential alternatives to toxic Pb^{2+} atoms. The stable tetravalent (+4) oxidation state of various transition and non-transition metal cations can further tune the optoelectronics of VOHPs through materials screening. Note that in the conventional ABX_3 where B = Sn, Ge encounters severe autoxidation of B^{2+} cations to B^{4+}, eventually leading to decomposition of the crystal structure.[18,19] For such systems, the vacancy-ordered form exhibits much higher stability as B remains at the tetravalent state, effectively resolving the issue of autoxidation-induced material instability.[16,17,20]

The family of A_2BX_6 perovskites exhibits distinctive physical and electronic features such as high compressibility,[21] reduced electronic band gaps,[22] and highly tunable emission proper-

Received: January 31, 2024
Revised: March 24, 2024
Accepted: March 25, 2024
Published: April 5, 2024

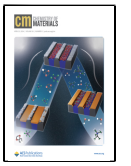

ties.[15,23] These attractive optoelectronic properties have already demonstrated promising applications of VOHPs in photovoltaics,[16,20] white-light emission,[24] thermoelectrics,[25] and photocatalysis.[17,26] Lee et al. have demonstrated Cs_2SnI_6 as an efficient hole transport layer in dye-sensitized solar cell devices under ambient conditions.[16] The defect tolerance of compositionally mixed Sn/Te-based VOHPs has been explored by Maughan et al.[27] The promising structural stability with a suitable band gap range (1.25−1.30 eV) demonstrates the possibility of fabricating optoelectronic devices from VOHPs. In recent work, some of us have computationally depicted the stable photocatalytic activity of MA_2SnBr_6 (MA, methylammonium) that has been synthesized successfully.[17] The strategic doping of VOHPs has successfully demonstrated widely tunable bright emission properties, indicating their applications in the display industry.[23,24] Though the initial reports are encouraging, the optoelectronic devices from VOHPs have yet to be significantly optimized for efficient performance.

The lack of chemically connected metal halide octahedra in VOHPs gives rise to intrinsic structural confinement, mitigating conventional charge carrier pathways.[28] Furthermore, the isolated metal halide octahedra exhibit more lattice dynamical activity than traditional MHPs, resulting in unique electron−phonon interactions in VOHPs.[29] The lattice dynamics under ambient conditions play a crucial role in determining the functional properties of MHPs, including carrier transport,[30] emission efficiency,[31] thermal conductivity,[32] and ferroelectricity.[33] In this regard, A cations that stack the isolated octahedra can indirectly influence the optoelectronic and transport properties of VOHPs.[29] Specifically, the A cations are typically distant from the electronic band edge states in these perovskites; however, dynamic coupling of those with inorganic octahedra can substantially impact the overall photophysics. Maughan et al. reported the anharmonic rattling of A-site cations under ambient conditions, inducing dynamic tilting in stand-alone $SnBr_6$ octahedra.[29] The A-cation size and its dynamic noncovalent interactions with octahedra modify the close-packed arrangement of halogen, impacting the electronic dispersions and carrier transport through the band edge states.[34] Moreover, several detailed studies have shown that the dynamic coupling between A cations and inorganic octahedra in MHPs influences the electron−phonon interactions, ultimately impacting excited state properties such as carrier recombination processes and carrier lifetimes.[29,34,35] Despite the substantial impact of these cations on the overall vibrational and excited state properties of VOHPs, an in-depth understanding of the correlation among structural dynamics, transient electronic structures, and carrier recombination properties is still largely lacking. Such insights are particularly essential for proposing fundamental design principles for VOHPs with efficient optoelectronic properties.

ML models can be utilized to develop strategic design principles and reveal underlying physical phenomena inside halide perovskites.[36−38] Here, we combine state-of-the-art atomistic modeling and unsupervised ML models to reveal the detailed impact of A cations on the dynamic electronic and excited state properties of VOHPs. This study considers three VOHPs, A_2SnBr_6, where A = Rb, Cs, or methylammonium (MA), where the A-site cations have varying cationic sizes and nonbonding interaction patterns with metal bromide octahedra. The computed structural dynamics show that the A cations significantly impact the geometric fluctuations and coupling with electronic states under ambient conditions. The non-adiabatic molecular dynamics (NAMD) simulations further depict that the nonradiative recombination rate of charge carriers strongly depends on the A cations in VOHPs. The ML-based analyses highlight the detailed dynamic geometry−optoelectronic property relationships by illustrating the correlation between the transient electronic properties and different structural features. We emphasize the importance of choosing appropriate A cations for the strategic design of efficient VOHPs with exceptional optoelectronic characteristics.

RESULTS AND DISCUSSION

Static Structural Properties. The computationally optimized structures of all three VOHPs retain their experimental geometry.[39,40] The optimized cell parameters agree with the available reported values (see Figure 1 and Figure S1).[17,20] Moving from Rb_2SnBr_6 to Cs_2SnBr_6 to MA_2SnBr_6, we found the optimized structures exhibit increased unit cell volumes. The lattice volume increases by 24.5% when Cs atoms are replaced with MA cations in these perovskites. This A-cation-induced lattice expansion is much more drastic for VOHPs than for three-dimensional (3D) MHPs, which expand their volume by only 5.4% when considering $CsSnBr_3$ and $MASnBr_3$.[41] The averaged Sn−Br distances and intra-octahedral Br−Br distances (Table S1) remain mostly unchanged in these VOHPs, depicting negligible impacts of A cations on the static internal structure of $SnBr_6$ octahedra. The increased ionic radii of the A cations expand the VOHP lattices systematically. The disconnected $SnBr_6$ octahedra move away from each other to accommodate large A-site cations, ultimately increasing the lattice volume.

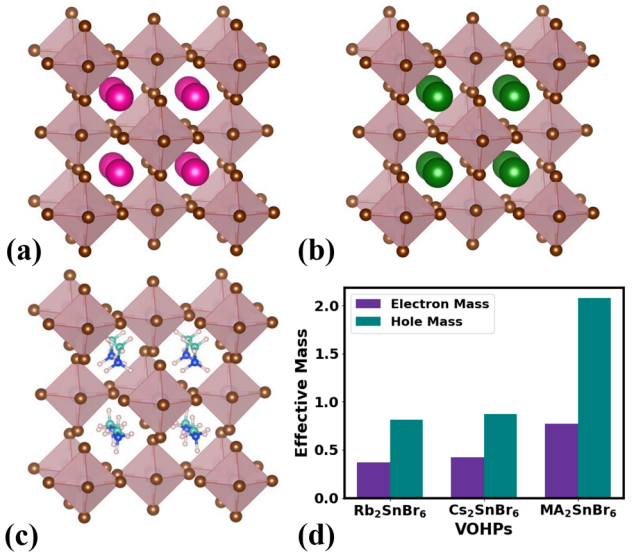

Figure 1. Schematics of optimized structures for (a) Rb_2SnBr_6, (b) Cs_2SnBr_6, and (c) MA_2SnBr_6. Key: brown for bromine (Br), silver for tin (Sn), pink for rubidium (Rb), green for cesium (Cs), white for hydrogen (H), cyan for carbon (C), and blue for nitrogen (N). (d) Bar plot representing the effective masses of the lightest electron and hole of all three VOHPs [along the Γ → X direction for $(Cs/Rb)_2SnBr_6$ and along the Γ → Y direction for MA_2SnBr_6].

Static Electronic Properties. The electronic structure calculations considering a hybrid functional (HSE06) and

https://doi.org/10.1021/acs.chemmater.4c00290
Chem. Mater. 2024, 36, 3875−3885

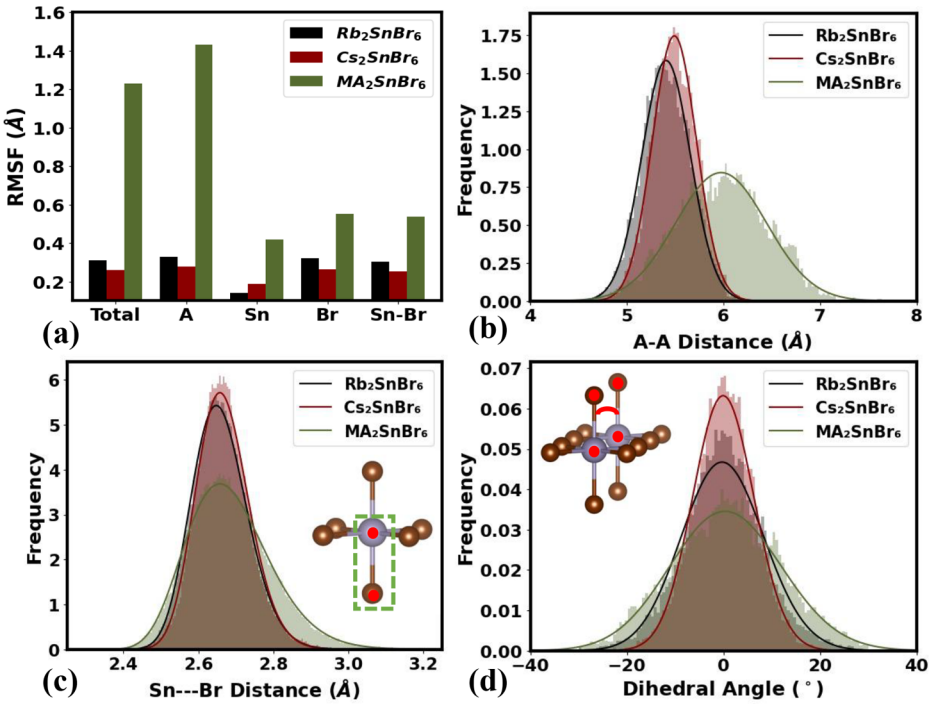

Figure 2. Impact of A-site cations on the structural dynamics in VOHPs under ambient conditions (300 K). (a) Bar chart of root-mean-square fluctuation (RMSF) values for whole systems (Total), the A-site cation (A), Sn, Br, and inorganic octahedra (Sn−Br) for all three perovskites. Histogram distribution plots of (b) distances (angstroms) between nearby A-site cations, (c) distances (angstroms) between intra-octahedral Sn and Br, and (d) dihedral angles between two Sn−Br bonds (along the *c*-axis) of two consecutive $SnBr_6$ octahedra. The insets of panels c−d represent the schematics of the plotted corresponding geometric parameters. Γ functions are used to fit the distribution data in panels b−d.

spin−orbit coupling (SOC) afford band gap values of 2.11 2.24, and 2.37 eV for Rb_2SnBr_6, Cs_2SnBr_6, and MA_2SnBr_6, respectively. The trends in the change in the band gap going from inorganic to organic and from a smaller to larger A-site cation in Sn-based VOHPs are consistent with experimentally reported values.[41] The partial density of states (pDOS) (Figure S2a−c) and charge densities of band edge states (Figure S3a−f) reveal that only the inorganic Sn−Br framework contributes to the edge states (consistent with traditional 3D halide perovskites).[17,42] The dominant contribution for the valence band maxima (VBM) is from nonbonding 4p orbitals of bromine, whereas the conduction band minimum (CBM) consists of mostly antibonding 5s orbitals of Sn and 4p orbitals of Br. Similar to traditional 3D halide perovskites, the A-site cation in VOHPs does not make a direct electronic contribution to the band edge states.[41,43] However, A-site cations indirectly influence band edge positions, resulting in a marginal variation of band gaps in these VOHPs.

The band structures of VOHPs are plotted (Figure S4) to understand the electronic dispersions in the Brillouin zone. All of the VOHPs show a direct band gap at the Γ point, agreeing well with the previous reports.[17,44,45] Moreover, the direction-dependent band dispersion trends are apparent in these band structure diagrams (Figure S4). The inter-octahedral Br···Br and Sn···Sn distance increases with A-site cation size from Rb to Cs to MA. These increased Br···Br distances result in a decrease in the level of conduction band dispersion, as shown in Figure S4. Nevertheless, the Sn−Br interactions exhibit very minor changes throughout the VOHPs (Table S1). Thus, the blue-shift of the band gap can be attributed to the variations in the close-packing arrangement of the Br sublattice, leading to alterations in the conduction band dispersion upon substitution of larger A-site cations, like MA.[29] To further investigate the influence of A-site cations on carrier transport, we evaluated the effective carrier masses. Figure 1d and Table S2 illustrate that MA_2SnBr_6 possesses carrier masses greater than those for Rb_2SnBr_6 and Cs_2SnBr_6. The A-cation-dependent effective masses are much more prominent for holes than for electrons. As the VBM band dispersion occurs due to Br···Br through-space interactions, the increased inter-octahedral halogen−halogen distances substantially flatten the band edge, increasing the hole effective mass in MA_2SnBr_6. It is worth mentioning that the effective masses of MHP are relatively much lower than those of their VOHP counterparts due to the lack of octahedral connectivity in an inorganic framework.[46] Moreover, the carrier effective masses in these 3D MHPs negligibly depend on the A cations.[47] Thus, the A cations influence the static electronic properties of VOHPs more significantly than those in traditional bulk MHPs.

Dynamic Structural Properties. The *ab initio* molecular dynamics (AIMD) simulations elucidate time-dependent structural fluctuations in VOHP lattices. The root-mean-square fluctuations (RMSF) plot in Figure 2a represents the thermal fluctuation of individual entities and the overall structure of the VOHPs. The total RMSF diminishes substantially from MA_2SnBr_6 to Rb_2SnBr_6 to Cs_2SnBr_6. Thus, the overall structural dynamics under ambient conditions strongly depend on the A-site cations. Note that Cs_2SnBr_6 (RMSF = 0.261 Å) is less dynamic than Rb_2SnBr_6 (RMSF = 0.512 Å), suggesting a more compact structure of Cs-based VOHPs. The RMSF plots also depict that highly dynamic MA cations interact with $[SnBr_6]^{2-}$ through noncovalent interactions, resulting in large structural fluctuations in the MA_2SnBr_6 (RMSF = 1.784 Å) perovskite. The detailed

https://doi.org/10.1021/acs.chemmater.4c00290
Chem. Mater. 2024, 36, 3875−3885

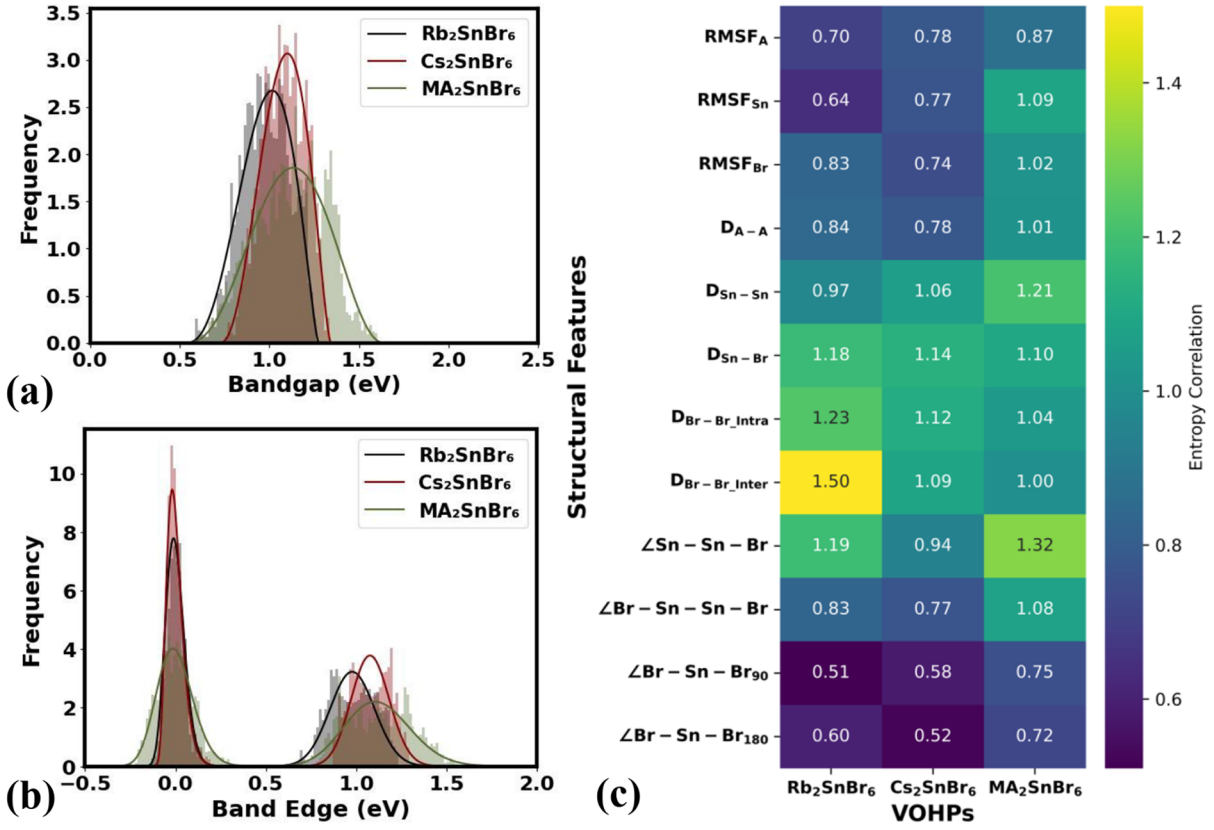

Figure 3. Electronic structures fluctuate over a 5 ps (5000 snapshots) time window for all three VOHPs at 300 K. Histogram plots for (a) band gaps and (b) the VBM and CBM state energies along the AIMD trajectories of corresponding VOHPs. (c) Mutual information of band gap with considered key structural features. For panel b, the energies of all of the electronic states are scaled to the average of the VBM state, which is at E = 0 eV.

RMSF values are listed in Table S3. Thus, the lattice fluctuations of these VOHPs under ambient conditions can be tuned by choosing the appropriate type and size of A-site cations.

We further explored the impact of thermal fluctuations on key structural parameters that directly or indirectly influence the optoelectronic properties of VOHPs. The dynamic distances between two A cations are presented as the histogram plot in Figure 2b. The MA−MA cation distances in MA_2SnBr_6 fluctuate much more than the A−A distances in inorganic VOHPs. The MA cations undergo flipping and wobbling rotational motions inside the loosely packed VOHP lattice.[48,49] Moreover, the light hydrogen atoms of MA cations exhibit a large extent of thermal fluctuations (Figure S5a,b). These relatively drastic molecular motions collectively broaden the MA−MA distance distribution with a greater standard deviation (SD) of 0.47 Å (Figure 2b). The relatively much heavier inorganic elemental monocations have limited dynamical activities inside the VOHP lattices (Figure S6) and exhibit a significantly narrower distribution of Cs−Cs (SD of 0.23 Å) or Rb−Rb (SD of 0.25 Å) distances over time (Figure 2b).

We categorize intra- and inter-octahedral fluctuations to explore the complex octahedral dynamics in these perovskites systematically. The Sn−Br bond distances in $SnBr_6$ along the AIMD trajectories are calculated and plotted in Figure 2c. The Sn−Br distribution captures the intra-octahedral thermal fluctuations in VOHPs under ambient conditions. Figure 2c depicts that the metal halide bond distances possess a narrower distribution in inorganic VOHPs than in MA_2SnBr_6 (SD of 0.112 Å). Close inspection further reveals that Sn−Br bond lengths fluctuate marginally less in Cs_2SnBr_6 (SD of 0.070 Å) than in Rb_2SnBr_6 (SD of 0.074 Å). The distribution of intra-octahedral Br−Sn−Br angles over time is also noticeably broader (SD of 5.65°) for MA-based VOHPs than for the other inorganic ones (SD of ∼3.86°) (Figure S7a). These structural parameters unambiguously depict that the A cations dynamically influence the intra-octahedral geometric features of $SnBr_6$ units. Note that such a substantial impact of A cations on the intra-octahedral dynamics in VOHPs sharply contrasts with that in the 3D MHPs, as reported previously.[50,51] Thus, unlike those of conventional 3D halide perovskites, the intra-octahedral motions in VOHPs can be largely fine-tuned by choosing appropriate A cations.

Focusing on the inter-octahedral dynamics in VOHPs, we first consider the dihedral angle between two consecutive $SnBr_6$ octahedra by tracking their mutual fluctuations over time. The dihedrals are calculated as the angle between planes that contain Sn−Br bonds along the same axes of the two nearest octahedra (see the inset of Figure 2d). The distributions of angles depict the following trend: MA_2SnBr_6 (SD of 11.55°) > Rb_2SnBr_6 (SD of 8.54°) > Cs_2SnBr_6 (SD of 6.31°). We also evaluate the dynamic Sn−Sn−Br tilt angles in these perovskites (see the inset of Figure S7b). The tilt angles capture the deviation of the Sn−Br bond from the inter-octahedral Sn−Sn axis. In a high-symmetry static structure, the tilt angle is 0° for all cubic VOHPs. Figure S7b shows a heightened peak with a narrower distribution (SD of 2.29°) of

https://doi.org/10.1021/acs.chemmater.4c00290
Chem. Mater. 2024, 36, 3875−3885

tilt angles in Cs_2SnBr_6 than in other VOHPs (SDs for Rb_2SnBr_6 of 3.08° and for MA_2SnBr_6 of 4.12°). We plot the intra- and inter-octahedral Br−Br and Sn−Sn distance distributions in Figures S7c,d and S8a to capture the distance parameter fluctuations. These analyses further depict that MA_2SnBr_6 experiences a range of halogen−halogen and metal−metal distances that are much more comprehensive than those in inorganic VOHPs.

At the atomistic level, hydrogen bond-mediated coupled motion between MA and $SnBr_6$ gives rise to the dynamic lattice in MA_2SnBr_6. The hydrogen bonds between H of MA and Br, i.e., $Br\cdots H_{MA}$, fluctuate drastically over time as MA has several active dynamic modes (Figure S5a). These relatively weak noncovalent interactions make the overall lattice, including intra-octahedral parameters, fluctuate more than that in inorganic VOHPs.

The anharmonicity in lattice dynamics under ambient conditions and its impact on the electronic properties of VOHPs have been explored by Maughan et al.[29] Our close inspection of MD trajectories also reveals several signatures of anharmonic lattice fluctuations and their dependence on the A cations of these perovskites. Unlike those of inorganic VOHPs, the intra-octahedral Sn−Br distance distributions exhibit an asymmetric peak with a tail on the long distance side for MA_2SnBr_6 (Figure 2c). The Br atoms form dynamic hydrogen bonds with MA cations, partially stabilizing the transient elongated Sn−Br bonds and introducing anharmonicity into the inorganic lattice. Such an asymmetric distribution of metal halide bond lengths has previously been demonstrated as a sign of anharmonic lattice fluctuations in 3D MHPs.[52] We further investigated the octahedral tilting (Sn−Sn−Br angle) distributions, which illustrate distinct asymmetric peaks for only hybrid VOHPs (Figure S7b). As indicated by Maughan et al., the asymmetric distribution of octahedral tilting also indicates the presence of hydrogen bond-induced anharmonic lattice fluctuations in MA_2SnBr_6.[29] Thus, these detailed analyses emphasize that A-cation motion significantly impacts the intra- and inter-octahedral dynamics in VOHPs.

Dynamic Electronic Properties. We computed the electronic structure of VOHPs over time to reveal the impact of structural dynamics on their photophysical properties. The band gap distributions are presented as the histogram plots in Figure 3a. The fluctuations of the band gap over time are also plotted in Figure S9a. The band gap distributions are evident in the dominant role of structural dynamics on the overall electronic structures of VOHPs. The more dynamic lattice of MA_2SnBr_6 has widely fluctuating band gaps with an SD of 0.19 eV. On the contrary, Cs_2SnBr_6, which has the least dynamic structure, exhibits the most narrowly (SD of 0.11 eV) distributed time-dependent band gap values (Figure 3a). We further investigate the variation in the individual band edge positions (Figure S8b) due to geometric fluctuations in these VOHPs. The rapid change in the VBM and CBM positions can modify the transient band alignment, ultimately impacting the charge carrier collection and transport in photovoltaic devices.[53] In Figure 3b, we plot the distributions of the relative energetic positions of the band edges over time. Because the Sn−Br framework dominantly contributes to the band edge states, the dynamic band edge position over the 5 ps time frame mainly depends upon the A-cation-induced Sn−Br fluctuation. Note that the Sn−Br sublattice of Cs_2SnBr_6 is less dynamic (Figure 2a) than those of Rb_2SnBr_6 and MA_2SnBr_6, indicating a more confined band edge distribution (Figure 3b). In addition, the CBM state fluctuates more drastically (SDs for Rb_2SnBr_6 of 0.12 eV, for Cs_2SnBr_6 of 0.10 eV, and for MA_2SnBr_6 of 0.18 eV), resulting in a distribution wider than that of the VBM state (SDs for Rb_2SnBr_6 of 0.054 eV, for Cs_2SnBr_6 of 0.047 eV, and for MA_2SnBr_6 of 0.099 eV) for all VOHPs. Thus, the phonon modes are strongly coupled to the CBM state under ambient conditions, changing their position rapidly on the femtosecond time scale. Among VOHPs, MA_2SnBr_6 exhibits the broadest distribution of varied band edge positions over time, reiterating the close dynamic structure−electronic property relationships.

The highly dynamic crystal lattices indicate the presence of several active phonon modes that can influence the transient electronic structures of VOHPs. Consequently, it becomes considerably challenging to identify the relevant features that most impact optoelectronics. In this regard, we compute mutual information (MI) that efficiently captures hard-to-find nonlinear correlations and provides a set of features that dominantly control the electronic structure fluctuations. These nontrivial correlations are revealed using the unsupervised ML algorithm of nonparametric entropy estimators, as detailed in previous works.[54,55]

To include diverse types of structural parameters, we track several geometric features such as RMSFs of atoms, intra- and inter-octahedral bond distances and angles, and dihedral angles throughout the simulation time and find the correlation with band gaps. In the heat map, Figure 3c, and Table S4, there are a few common trends that emerge from these MI analyses. The band gaps of these VOHPs share considerable mutual information with intra- and inter-octahedral Br−Br distances ($D_{Br-Br\_intra/inter}$). As the band edge states remain delocalized over the $SnBr_6$ octahedra, the high MI between intra-octahedral Br−Br distances and band gaps is expected and discussed further in section S4 of the Supporting Information. However, because these VOHPs have isolated octahedra, the high correlation between inter-octahedral Br−Br distances and band gaps is nontrivial. This insight emphasizes the through-space dynamic electronic coupling among the halogen orbitals of the neighboring octahedra that in turn controls the VBM−CBM energy gap. The features involving metal−halide octahedra, such as Sn−Sn−Br tilting angles (∠Sn−Sn−Br), Sn−Br distances (D_{Sn-Br}), and Sn−Sn shortest distances (D_{Sn-Sn}), also exhibit relatively a high correlation with band gaps.

Note that these features are mostly different from the feature set that exhibits a high MI with the band gap in traditional MHPs.[54,56] Thus, VOHPs have a dynamic structure−property relationship substantially dissimilar from that of MHPs. The presence of multiple inter-octahedral features illustrates that even though $SnBr_6$ octahedra are not chemically connected, their mutual dynamics significantly influence the band gap values of VOHPs. Further analysis identifies several structural features with a high MI with a band gap for only MA_2SnBr_6. Specifically, the features for A-cation dynamics, such as the A−A distance (D_{A-A}) and RMSF of A ($RMSF_A$), exhibit more correlation with the band gap in MA-based perovskites than inorganic ones. As A cations do not contribute directly to the band edge states, the high MI for these features is somewhat unexpected. We realize that the significant influence of the rattling motion of MA cations to the band edge states gives rise to such high MI values. The quantified MI between structural features and individual band edges further reveals that the VBM state is more correlated to the A-cation dynamics. A

https://doi.org/10.1021/acs.chemmater.4c00290
Chem. Mater. 2024, 36, 3875−3885

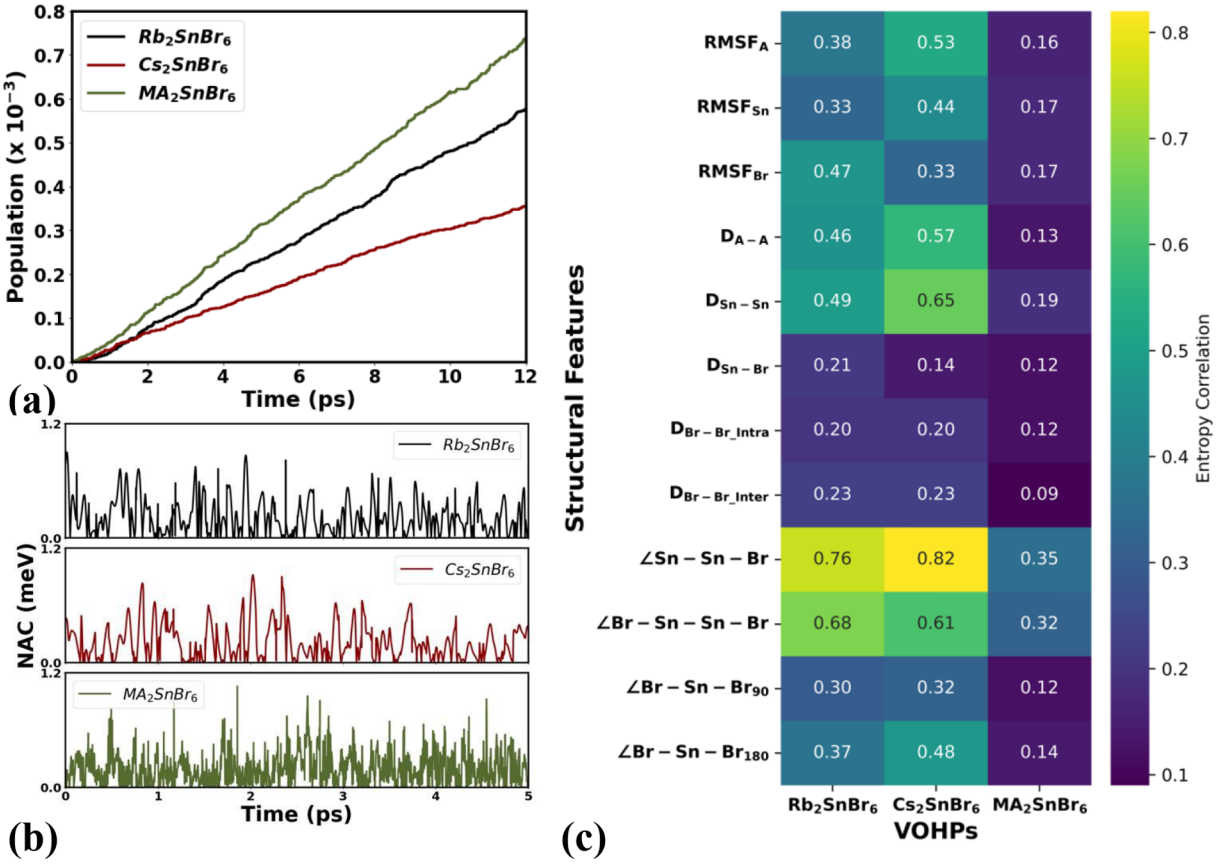

Figure 4. Excited state charge carrier dynamics in VOHPs under ambient conditions. (a) Population of non-radiatively recombined electron−hole over time in VOHPs. (b) Absolute NAC values between VBM and CBM energy states for a 5 ps time window under ambient conditions. (c) Mutual information of NAC with considered key structural features.

detailed discussion of the MI between band edges and structural features is included in section S4. The evaluated nonlinear correlations indicate that a more dynamic lattice of MA_2SnBr_6 results in a greater number of structural factors that modify the band gap values over time.

Excited State Dynamics. The thermal lattice fluctuations in MHPs substantially influence the photoexcited charge carrier dynamics activating nonradiative carrier recombination processes, which can reliably be modeled by combining the non-adiabatic molecular dynamics (NA-MD) with time-dependent density functional theory (TD-DFT).[57−59] The recombined carrier population along the NAMD trajectories illustrates faster nonradiative band-to-band charge recombination in MA_2SnBr_6 than in inorganic VOHPs (Figure 4a). Furthermore, the nonradiative recombination rate of Cs_2SnBr_6 is lower than that of Rb_2SnBr_6, depicting the subtle impact of A cations on charge carrier dynamics. Employing the short-time linear approximation to the exponential function, we evaluate the nonradiative carrier lifetimes as 21.12, 32.38, and 16.43 ns for Rb_2SnBr_6, Cs_2SnBr_6, and MA_2SnBr_6, respectively. Thus, the nonradiative carrier lifetime can be elongated 2-fold upon complete substitution of MA with Cs in A_2SnBr_6 perovskites. The nanosecond time scale for computed carrier lifetimes in MHPs closely agrees with experimental reports.[60,61] Our findings emphasize the pivotal role of the A cation in tuning the excited state carrier dynamics of VOHPs, indicating a strategic approach for enhancing their efficiency for photovoltaics and LED applications.

Nonradiative recombination serves as the predominant pathway for the dissipation of charges and energy, thereby constraining the efficiency of photon-to-electron conversion in perovskite solar cells. We computationally simulate radiative lifetimes to discern whether carrier lifetimes are constrained by nonradiative or radiative decay. The emission lifetime stands as the reciprocal of the Einstein coefficient (see Computational Methods for details). Our computed radiative recombination times for Rb_2SnBr_6, Cs_2SnBr_6, and MA_2SnBr_6 perovskites are 184.59, 153.01, and 147.61 ns, respectively. Notably, these time scales exceed the corresponding nonradiative electron−hole recombination times, as illustrated in Table 1. These findings reveal that the harvested electronic energy by photoexcitation dissipates to phonon modes much faster than the radiative process,[62−64] resulting in poor emission in pristine VOHPs.[65,66]

Table 1. Averaged Band Gaps over 5 ps Trajectories, Nonradiative Recombination Times, and Decoherence Times (VBM−CBM) for All of the VOHPs[a]

	Rb_2SnBr_6	Cs_2SnBr_6	MA_2SnBr_6
averaged band gap (eV)	0.98	1.08	1.12
nonradiative recombination lifetime (ns)	21.12	32.38	16.43
decoherence time (fs)	4.9	5.7	3.4

[a]The detailed methodology for the calculation is provided in Computational Methods. The averaged band gaps are calculated using semilocal exchange-correlation functionals.

https://doi.org/10.1021/acs.chemmater.4c00290
Chem. Mater. 2024, 36, 3875−3885

The dynamic interplay between electronic and lattice degrees of freedom exerts a dominant influence on nonradiative charge relaxation and recombination processes, significantly impacting the operational device efficacy of optoelectronic devices.[67,68] During nonradiative recombination, the excess energy of excited electrons dissipates through various active inelastic electron−phonon scattering processes. In contrast, the elastic electron−phonon modes can slow nonradiative decay by hampering the coherence between engaged states. The inelastic electron−phonon interaction that frequently plays a key role is quantified as non-adiabatic coupling (NAC).[69] We compute the NAC constants between the band edges along the simulated trajectories for evaluating the instantaneous inelastic scattering strength. Conceptually, an increased NAC value denotes a more robust coupling between electronic and lattice degrees of freedom, indicating accelerated nonradiative charge recombination in the material.[70] In Figure 4b, the NAC strengths along the MD trajectories highlight a few crucial factors. (a) MA_2SnBr_6 exhibits high instantaneous NAC values (>0.5 meV) more frequently than the inorganic ones, and (b) the NAC values fluctuate much faster in time for hybrid VOHPs. The large number of high instantaneous NAC values indicates more regular opening of non-adiabatic channels, giving rise to a faster rate of nonradiative band-to-band carrier recombination in MA_2SnBr_6. Moreover, the Fourier transformation (FT) of NACs over time (Figure S9b) illustrates that there is a broader range of frequencies for MA_2SnBr_6, emphasizing its more active inelastic electron−phonon interaction processes. The large number of peaks in the FT plot also indicates that there are various phonon modes that couple to the band edge states, impacting the instantaneous NAC strengths. In this regard, Rb_2SnBr_6 also exhibits several higher frequencies but much less than MA-based VOHPs. We thus rationalize that the strength and variation of NACs over time have dominant control over the nonradiative charge carrier recombination rates in VOHPs.

Due to their significant influence on the excited state carrier dynamics, we further evaluate the shared information between NACs and several dynamical structural parameters in terms of MI. Figure 4c and Table S7 show that MI values are much smaller for MA_2SnBr_6 than for inorganic VOHPs, indicating weaker correlations between structural features and NAC values. The drastic fluctuations of instantaneous NACs and structural features over time collectively reduce the shared information in this dynamic system. Considering several features, NAC appears to be most correlated with ∠Sn−Sn−Br for all VOHPs (see Table S8 for a detailed description of considered key structural features). Additionally, the Br−Sn−Sn−Br dihedral angles (∠Br−Sn−Sn−Br) in inorganic VOHPs also share considerably adequate information with instantaneous NACs. The entropy correlation between inter-octahedral features and NACs emphasizes the dominant impact of collective tilting motions in chemically disconnected $SnBr_6$ on electron−phonon interaction strengths. The octahedral tilting motion shows a higher correlation with NAC in 3D MHPs, as well.[55,71] Other inter-octahedral distance features, such as D_{A-A} and D_{Sn-Sn}, correlate with NACs in Cs- and Br-based perovskites. Note that the A-cation-related features (D_{A-A} and $RMSF_A$) illustrate a decrease in MI moving from Cs to Rb to MA as the A site in VOHPs. Thus, more fluctuation of A-site cations results in a weaker correlation between these features and NAC values.

We further calculate the FT of the unnormalized autocorrelation function of electronic band gap evolution over time, yielding the influence spectra. These spectra unveiled distinct phonon modes that actively engage with the dynamic electronic subsystems, playing a pivotal role in interband electron−hole recombination. In Figure S10a, the dominant active phonon modes governing band edge fluctuations appear in the range of 150−200 cm^{-1}. These modes originate from the stretching of intra-octahedral Sn−Br bonds in $SnBr_6$ units. The spectral details are largely consistent with the experimental findings from Raman spectroscopy for Cs_2SnBr_6.[22] The differences in the influence spectra become apparent at the higher-frequency range, indicating a substantial influence of the A-site cation on the dynamics of excited state carriers. MA_2SnBr_6 exhibits higher-frequency modes at >225 cm^{-1}, originating from coupled MA−$SnBr_6$ motions. These modes are largely absent in inorganic ligands $(Rb/Cs)_2SnBr_6$. The presence of a broad range of active phonon modes in the influence spectra further depicts the overall more dynamic lattice of MA_2SnBr_6. Focusing on inorganic VOHPs, we further find that Rb_2SnBr_6 has more active phonon modes at >250 cm^{-1}, indicating active rattling motions of smaller Rb cations in the void spaces. The relatively large Cs cations fit well in the designated site and illustrate the least dynamical activity under ambient conditions. Overall, we find that the A-cation dynamics and their coupling with inorganic octahedra considerably impact the electron−phonon interactions in VOHPs. A-cation-dynamics-dependent anharmonic Sn−Br octahedral fluctuation significantly determines the active phonon modes for nonradiative recombination of photo-induced excited charge carriers. This behavior focuses on the significance of structural dynamics in shaping the electronic properties of A_2SnBr_6 VOHPs.

Pure decoherence accounts for the destruction of quantum coherence due to elastic electron−phonon scattering (see section S5 for a detailed computational methodology). A rapid quantum decoherence over time, typically on the femtosecond scale, diminishes the transition probability and extends the lifetime of a specific quantum state. In the context of electron−phonon recombination at semiconductor band edges, a quicker decoherence between the VBM and CBM corresponds to a prolonged recombination time. The calculated dephasing times for VOHPs, as included in Table 1, are in the range of 3.4−5.7 fs, depicting the ultrafast decoherence process (Figure S10b). Because of the very similar quantum decoherence times for all considered VOHPs, we realize that such a process does not play a crucial role in the considerably different carrier lifetimes in these perovskites.

Our detailed study investigates several features like band gap distribution, instantaneous NAC strengths over time, and decoherence processes that can play key roles in controlling the charge carrier dynamics and recombination in VOHPs. Considering the relative importance of these factors, Fermi's golden rule states that the band-to-band recombination rate should be proportional to the square of NAC strength and inversely proportional to the energy gap between the involved electronic states. The marginally blue-shifted band gap distribution of MA_2SnBr_6 compared to those of its inorganic counterparts depicts that the non-adiabatic processes dominate the nonradiative charge recombination here. The frequent large instantaneous values and rapid fluctuations of NAC over time give rise to a much faster carrier recombination rate for MA-based VOHPs. The highly dynamic MA cations in the

https://doi.org/10.1021/acs.chemmater.4c00290
Chem. Mater. 2024, 36, 3875−3885

voids of VOHPs cause large spikes in NAC values over time, facilitating interband charge relaxation.

CONCLUSION

In conclusion, our extensive study unambiguously identifies the decisive impact of A-cation dynamics on the excited state charge carrier dynamics in VOHPs. The initial static structure and electronic properties illustrate the negligible impact of the A cations. However, AIMD simulations show the significant impact of A cations on the dynamic structural and optoelectronic characteristics of these VOHPs. The detailed unsupervised ML analyses efficiently establish the complex nonlinear correlations between dynamic structural features and material properties like the band gap and NACs. Though these VOHPs contain isolated $SnBr_6$ octahedra, the inter-octahedral dynamical features like tilting, dihedral angles, and Sn−Sn distances exhibit high MI values with band gaps and NACs. These insights firmly state that initial attempts to understand the optoelectronics and emission from VOHPs by focusing only on the individual octahedra are insufficient. The MA cations that activate several phonon modes in MA_2SnBr_6 give rise to large instantaneous NACs, ultimately accelerating the nonradiative charge carrier recombination processes. From this work, we suggest considering inorganic elemental monocations such as Cs^+ to realize high-performance VOHPs for optoelectronic applications. The elaborate understanding of the complex and noncolinear structure−property relationships can provide strategic design principles for further improvement of the photophysical properties of MHPs.

COMPUTATIONAL METHODS

All of the DFT-based calculations, along with AIMD simulations, were performed using the Vienna Ab Initio Simulation Package (VASP) with a projector-augmented wave (PAW) approach to describe the interaction of ion and valence electrons.[72−75] The cutoff energy of 520 eV was considered for the plane wave basis set to relax the vacancy-ordered perovskite structures. The energy convergence criterion was set to 10^{-6} eV, and the geometry was relaxed until the Hellmann−Feynman force between ions reached <0.01 eV/Å. Moreover, geometry relaxation has been done where coordinates of atoms along with cell shape and volume were allowed to relax (setting ISIF = 3 in VASP INCAR). For exchange-correlation interaction, the semilocal generalized gradient approximation (GGA) functional in the form of Perdew−Burke−Ernzerhof (PBE) has been considered for geometry optimization simulations.[76] We have taken Γ-centered 3 × 3 × 3 Monkhorst−Pack k-point mesh and included dispersion correction DFT-D3 as Grimme et al. prescribed for these simulations.[77,78] Screened hybrid functionals of Heyd−Scuseria−Ernzerhof (HSE06) and the spin−orbit coupling (SOC) effects were considered to calculate the electronic structures with reasonable accuracy. We have used SUMO to analyze the electronic properties of these halide perovskites.[79] Moreover, VESTA and VMD have been used for static and dynamic structural bond parameter calculations, respectively.[80,81] A detailed description of the methodology for AIMD, NAMD (using the PYXAID code),[82,83] and mutual information (MI)[84] is available in section S5.

ASSOCIATED CONTENT

Supporting Information

The Supporting Information is available free of charge at https://pubs.acs.org/doi/10.1021/acs.chemmater.4c00290.

Unit cell structure, structural parameters, electronic properties (PDOS, charge density plot, band structure, and effective mass), dynamic structure (RMSF values, radial distribution, A−A distance fluctuation, and histogram distribution of dynamic structural parameters), instantaneous band gap fluctuation plot, FT autocorrelation of an instantaneous NAC plot, spectral density plot, decoherence time, mutual information on band edge states, MI values, description of all structural features, detailed computational methods, and additional references (PDF)

AUTHOR INFORMATION

Corresponding Author

Dibyajyoti Ghosh − *Department of Chemistry, Indian Institute of Technology, New Delhi 110016, India; Department of Materials Science and Engineering, Indian Institute of Technology, New Delhi 110016, India;* orcid.org/0000-0002-3640-7537; Email: dibyajyoti@iitd.ac.in, dibyajnc@gmail.com

Authors

Pabitra Kumar Nayak − *Department of Chemistry, Indian Institute of Technology, New Delhi 110016, India*

Carlos Mora Perez − *Department of Chemistry, University of Southern California, Los Angeles, California 90089, United States;* orcid.org/0000-0001-8840-5093

Dongyu Liu − *HSE University, 101000 Moscow, Russia*

Oleg V. Prezhdo − *Department of Chemistry, University of Southern California, Los Angeles, California 90089, United States; Department of Physics & Astronomy, University of Southern California, Los Angeles, California 90089, United States;* orcid.org/0000-0002-5140-7500

Complete contact information is available at: https://pubs.acs.org/10.1021/acs.chemmater.4c00290

Notes

The authors declare no competing financial interest.

ACKNOWLEDGMENTS

P.K.N. thanks the Department of Education, Government of India, for the Prime Minister's Research Fellowship (PMRF ID 1402687). D.G. acknowledges IIT Delhi SEED Grant PLN12/04MS, the Science and Engineering Research Board (SERB), Department of Science and Technology (DST), India, for Start-up Research Grant SRG/2022/001234, the CSIR-Human Resource Development Group (HRDG) for ExtraMural Research-II Grant 01/3136/23/EMR-II, and the IIT Delhi HPC facility for computational resources. This work was performed, in part, at the Center for Integrated Nanotechnologies, an Office of Science User Facility operated for the U.S. Department of Energy (DOE) Office of Science by Los Alamos National Laboratory (Contract 89233218CNA000001) and Sandia National Laboratories (Contract DE-NA-0003525). C.M.P. and O.V.P. acknowledge funding from U.S. National Science Foundation Grant CHE-2154367.

REFERENCES

(1) Yoo, J. J.; Seo, G.; Chua, M. R.; Park, T. G.; Lu, Y.; Rotermund, F.; Kim, Y. K.; Moon, C. S.; Jeon, N. J.; Correa-Baena, J. P.; Bulović, V.; Shin, S. S.; Bawendi, M. G.; Seo, J. Efficient Perovskite Solar Cells via Improved Carrier Management. *Nature* **2021**, *590* (7847), 587−593.

(2) Correa Baena, J. P.; Steier, L.; Tress, W.; Saliba, M.; Neutzner, S.; Matsui, T.; Giordano, F.; Jacobsson, T. J.; Srimath Kandada, A. R.; Zakeeruddin, S. M.; Petrozza, A.; Abate, A.; Nazeeruddin, M. K.;

Grätzel, M.; Hagfeldt, A. Highly Efficient Planar Perovskite Solar Cells through Band Alignment Engineering. *Energy Environ. Sci.* **2015**, *8* (10), 2928−2934.
(3) Sun, Y.; Ge, L.; Dai, L.; Cho, C.; Ferrer Orri, J.; Ji, K.; Zelewski, S. J.; Liu, Y.; Mirabelli, A. J.; Zhang, Y.; Huang, J. Y.; Wang, Y.; Gong, K.; Lai, M. C.; Zhang, L.; Yang, D.; Lin, J.; Tennyson, E. M.; Ducati, C.; Stranks, S. D.; Cui, L. S.; Greenham, N. C. Bright and Stable Perovskite Light-Emitting Diodes in the near-Infrared Range. *Nature* **2023**, *615* (7954), 830−835.
(4) Liu, Y.; Dong, Y.; Zhu, T.; Ma, D.; Proppe, A.; Chen, B.; Zheng, C.; Hou, Y.; Lee, S.; Sun, B.; Jung, E. H.; Yuan, F.; Wang, Y. K.; Sagar, L. K.; Hoogland, S.; García De Arquer, F. P.; Choi, M. J.; Singh, K.; Kelley, S. O.; Voznyy, O.; Lu, Z. H.; Sargent, E. H. Bright and Stable Light-Emitting Diodes Based on Perovskite Quantum Dots in Perovskite Matrix. *J. Am. Chem. Soc.* **2021**, *143* (38), 15606−15615.
(5) Zhu, X.; Lin, Y.; San Martin, J.; Sun, Y.; Zhu, D.; Yan, Y. Lead Halide Perovskites for Photocatalytic Organic Synthesis. *Nature Communications 2019 10:1* **2019**, *10* (1), 1−10.
(6) Huang, H.; Pradhan, B.; Hofkens, J.; Roeffaers, M. B. J.; Steele, J. A. Solar-Driven Metal Halide Perovskite Photocatalysis: Design, Stability, and Performance. *ACS Energy Lett.* **2020**, *5* (4), 1107−1123.
(7) Feng, J.; Gong, C.; Gao, H.; Wen, W.; Gong, Y.; Jiang, X.; Zhang, B.; Wu, Y.; Wu, Y.; Fu, H.; Jiang, L.; Zhang, X. Single-Crystalline Layered Metal-Halide Perovskite Nanowires for Ultrasensitive Photodetectors. *Nature Electronics 2018 1:7* **2018**, *1* (7), 404−410.
(8) Li, H.; Song, J.; Pan, W.; Xu, D.; Zhu, W.-a.; Wei, H.; Yang, B. Sensitive and Stable 2D Perovskite Single-Crystal X-Ray Detectors Enabled by a Supramolecular Anchor. *Adv. Mater.* **2020**, *32* (40), 2003790.
(9) Manser, J. S.; Christians, J. A.; Kamat, P. V. Intriguing Optoelectronic Properties of Metal Halide Perovskites. *Chem. Rev.* **2016**, *116* (21), 12956−13008.
(10) Smith, M. D.; Connor, B. A.; Karunadasa, H. I. Tuning the Luminescence of Layered Halide Perovskites. *Chem. Rev.* **2019**, *119* (5), 3104−3139.
(11) Li, J.; Cao, H. L.; Jiao, W.-B.; Wang, Q.; Wei, M.; Cantone, I.; Lü, J.; Abate, A. Biological Impact of Lead from Halide Perovskites Reveals the Risk of Introducing a Safe Threshold. *Nat. Commun.* **2020**, *11* (1), 310.
(12) Chowdhury, T. A.; Bin Zafar, M. A.; Sajjad-Ul Islam, M.; Shahinuzzaman, M.; Islam, M. A.; Khandaker, M. U. Stability of Perovskite Solar Cells: Issues and Prospects. *RSC Adv.* **2023**, *13* (3), 1787−1810.
(13) Singh, S.; Nayak, P. K.; Tretiak, S.; Ghosh, D. Composition Dependent Strain Engineering of Lead-Free Halide Double Perovskite: Computational Insights. *J. Phys. Chem. Lett.* **2023**, *14* (42), 9479−9489.
(14) Dey, K.; Ghosh, D.; Pilot, M.; Pering, S.; Roose, B.; Deswal, P.; Senanayak, S.; Cameron, P. J.; Islam, S.; Stranks, S. D. Substitution of Lead with Tin Suppresses Ionic Transport in Halide Perovskite Optoelectronics. *Energy Environ. Sci.* **2024**, *17*, 760−769.
(15) Folgueras, M. C.; Jiang, Y.; Jin, J.; Yang, P. High-Entropy Halide Perovskite Single Crystals Stabilized by Mild Chemistry. *Nature* **2023**, *621* (7978), 282−288.
(16) Lee, B.; Stoumpos, C. C.; Zhou, N.; Hao, F.; Malliakas, C.; Yeh, C. Y.; Marks, T. J.; Kanatzidis, M. G.; Chang, R. P. H. Air-Stable Molecular Semiconducting Iodosalts for Solar Cell Applications: Cs2SnI6 as a Hole Conductor. *J. Am. Chem. Soc.* **2014**, *136* (43), 15379−15385.
(17) Rawat, B.; Battula, V. R.; Nayak, P. K.; Ghosh, D.; Kailasam, K. Utilizing the Undesirable Oxidation of Lead-Free Hybrid Halide Perovskite Nanosheets for Solar-Driven Photocatalytic C(sp^3)−H Activation: Unraveling the Serendipity. *ACS Appl. Mater. Interfaces* **2023**, *15* (46), 53604−53613.
(18) Nasti, G.; Abate, A. Tin Halide Perovskite (ASnX3) Solar Cells: A Comprehensive Guide toward the Highest Power Conversion Efficiency. *Adv. Energy Mater.* **2020**, *10* (13), 1902467.
(19) Krishnamoorthy, T.; Ding, H.; Yan, C.; Leong, W. L.; Baikie, T.; Zhang, Z.; Sherburne, M.; Li, S.; Asta, M.; Mathews, N.; Mhaisalkar, S. G. Lead-Free Germanium Iodide Perovskite Materials for Photovoltaic Applications. *J. Mater. Chem. A Mater.* **2015**, *3* (47), 23829−23832.
(20) Kaltzoglou, A.; Antoniadou, M.; Kontos, A. G.; Stoumpos, C. C.; Perganti, D.; Siranidi, E.; Raptis, V.; Trohidou, K.; Psycharis, V.; Kanatzidis, M. G.; Falaras, P. Optical-Vibrational Properties of the Cs2SnX6 (X = Cl, Br, I) Defect Perovskites and Hole-Transport Efficiency in Dye-Sensitized Solar Cells. *J. Phys. Chem. C* **2016**, *120* (22), 11777−11785.
(21) Wang, L.; Yao, P.; Wang, F.; Li, S.; Chen, Y.; Xia, T.; Guo, E.; Wang, K.; Zou, B.; Guo, H. Pressure-Induced Structural Evolution and Bandgap Optimization of Lead-Free Halide Double Perovskite (NH4)2SeBr6. *Advanced Science* **2020**, *7* (6), 1902900.
(22) Karim, M. M. S.; Ganose, A. M.; Pieters, L.; Winnie Leung, W. W.; Wade, J.; Zhang, L.; Scanlon, D. O.; Palgrave, R. G. Anion Distribution, Structural Distortion, and Symmetry-Driven Optical Band Gap Bowing in Mixed Halide Cs2SnX6 Vacancy Ordered Double Perovskites. *Chem. Mater.* **2019**, *31* (22), 9430−9444.
(23) Chang, T.; Wei, Q.; Zeng, R.; Cao, S.; Zhao, J.; Zou, B. Efficient Energy Transfer in Te4+-Doped Cs2ZrCl6Vacancy-Ordered Perovskites and Ultrahigh Moisture Stability via A-Site Rb-Alloying Strategy. *J. Phys. Chem. Lett.* **2021**, *12* (7), 1829−1837.
(24) Zhong, Y.; Huang, Y. E.; Deng, T.; Lin, Y. T.; Huang, X. Y.; Deng, Z. H.; Du, K. Z. Multi-Dopant Engineering in Perovskite Cs2SnCl6: White Light Emitter and Spatially Luminescent Heterostructure. *Inorg. Chem.* **2021**, *60* (22), 17357−17363.
(25) Bhumla, P.; Jain, M.; Sheoran, S.; Bhattacharya, S. Vacancy-Ordered Double Perovskites Cs2BI6(B = Pt, Pd, Te, Sn): An Emerging Class of Thermoelectric Materials. *J. Phys. Chem. Lett.* **2022**, *13* (50), 11655−11662.
(26) Hamdan, M.; Manoj, M.; Halpati, J. S.; Chandiran, A. K. Acid- and Base-Stable Cs2Pt(Cl,Br)6 Vacancy-Ordered Double Perovskites and Their Core-Shell Heterostructures for Solar Water Oxidation. *Solar RRL* **2022**, *6* (7), 2101092.
(27) Maughan, A. E.; Ganose, A. M.; Bordelon, M. M.; Miller, E. M.; Scanlon, D. O.; Neilson, J. R. Defect Tolerance to Intolerance in the Vacancy-Ordered Double Perovskite Semiconductors Cs2SnI6 and Cs2TeI6. *J. Am. Chem. Soc.* **2016**, *138* (27), 8453−8464.
(28) Cucco, B.; Katan, C.; Even, J.; Kepenekian, M.; Volonakis, G. Fine Structure of Excitons in Vacancy-Ordered Halide Double Perovskites. *ACS Mater. Lett.* **2023**, *5* (1), 52−59.
(29) Maughan, A. E.; Ganose, A. M.; Candia, A. M.; Granger, J. T.; Scanlon, D. O.; Neilson, J. R. Anharmonicity and Octahedral Tilting in Hybrid Vacancy-Ordered Double Perovskites. *Chem. Mater.* **2018**, *30* (2), 472−483.
(30) Herz, L. M. How Lattice Dynamics Moderate the Electronic Properties of Metal-Halide Perovskites. *J. Phys. Chem. Lett.* **2018**, *9* (23), 6853−6863.
(31) Masada, S.; Yamada, T.; Tahara, H.; Hirori, H.; Saruyama, M.; Kawawaki, T.; Sato, R.; Teranishi, T.; Kanemitsu, Y. Effect of A-Site Cation on Photoluminescence Spectra of Single Lead Bromide Perovskite Nanocrystals. *Nano Lett.* **2020**, *20* (5), 4022−4028.
(32) Xie, H.; Hao, S.; Bao, J.; Slade, T. J.; Snyder, G. J.; Wolverton, C.; Kanatzidis, M. G. All-Inorganic Halide Perovskites as Potential Thermoelectric Materials: Dynamic Cation off-Centering Induces Ultralow Thermal Conductivity. *J. Am. Chem. Soc.* **2020**, *142* (20), 9553−9563.
(33) Ambrosio, F.; De Angelis, F.; Goñi, A. R. The Ferroelectric-Ferroelastic Debate about Metal Halide Perovskites. *J. Phys. Chem. Lett.* **2022**, *13* (33), 7731−7740.
(34) Maughan, A. E.; Ganose, A. M.; Scanlon, D. O.; Neilson, J. R. Perspectives and Design Principles of Vacancy-Ordered Double Perovskite Halide Semiconductors. *Chem. Mater.* **2019**, *31* (4), 1184−1195.
(35) Maughan, A. E.; Paecklar, A. A.; Neilson, J. R. Bond Valences and Anharmonicity in Vacancy-Ordered Double Perovskite Halides. *J. Mater. Chem. C* **2018**, *6* (44), 12095−12104.

https://doi.org/10.1021/acs.chemmater.4c00290
Chem. Mater. 2024, 36, 3875−3885

(36) Li, J.; Pradhan, B.; Gaur, S.; Thomas, J. Predictions and Strategies Learned from Machine Learning to Develop High-Performing Perovskite Solar Cells. *Adv. Energy Mater.* **2019**, *9* (46), 1901891.
(37) Srivastava, M.; Hering, A. R.; An, Y.; Correa-Baena, J. P.; Leite, M. S. Machine Learning Enables Prediction of Halide Perovskites' Optical Behavior with > 90% Accuracy. *ACS Energy Lett.* **2023**, *8* (4), 1716−1722.
(38) Cai, X.; Liu, F.; Yu, A.; Qin, J.; Hatamvand, M.; Ahmed, I.; Luo, J.; Zhang, Y.; Zhang, H.; Zhan, Y. Data-Driven Design of High-Performance MASnxPb1-XI3 Perovskite Materials by Machine Learning and Experimental Realization. *Light: Science & Applications 2022 11:1* **2022**, *11* (1), 1−12.
(39) Cheng, R.; Zeng, Z.; Wang, C.; Ouyang, N.; Chen, Y. Impact of Strain-Insensitive Low-Frequency Phonon Modes on Lattice Thermal Transport in A 2 X B 6 -Type Perovskites. *Phys. Rev. B* **2024**, *109* (5), 054305.
(40) Lai, C. F.; Chang, Y. C.; Tien, Y. C. Stable Lead-Free Cesium Tin Halide Double-Perovskite Nanocrystals Embedded in Poly-dimethylsiloxane for Candlelight Light-Emitting Diodes. *ACS Appl. Nano Mater.* **2021**, *4* (2), 1924−1931.
(41) Coduri, M.; Strobel, T. A.; Szafrański, M.; Katrusiak, A.; Mahata, A.; Cova, F.; Bonomi, S.; Mosconi, E.; De Angelis, F.; Malavasi, L. Band Gap Engineering in MASnBr3 and CsSnBr3 Perovskites: Mechanistic Insights through the Application of Pressure. *J. Phys. Chem. Lett.* **2019**, *10* (23), 7398−7405.
(42) Pitaro, M.; Tekelenburg, E. K.; Shao, S.; Loi, M. A. Tin Halide Perovskites: From Fundamental Properties to Solar Cells. *Adv. Mater.* **2022**, *34* (1), 2105844.
(43) Huang, L. Y.; Lambrecht, W. R. L. Electronic Band Structure, Phonons, and Exciton Binding Energies of Halide Perovskites CsSnCl3, CsSnBr3, and CsSnI3. *Phys. Rev. B* **2013**, *88* (16), 165203.
(44) Kavanagh, S. R.; Savory, C. N.; Liga, S. M.; Konstantatos, G.; Walsh, A.; Scanlon, D. O. Frenkel Excitons in Vacancy-Ordered Titanium Halide Perovskites (Cs2TiX6). *J. Phys. Chem. Lett.* **2022**, *13* (47), 10965−10975.
(45) Sreedevi, P. D.; Ravindran, P. Revealing the Optoelectronic Properties of Tin-Based Vacancy Ordered Double Perovskites: K2SnBr6and Rb2SnBr6. *AIP Conf. Proc.* **2021**, No. 1, 2369.
(46) Galkowski, K.; Mitioglu, A.; Miyata, A.; Plochocka, P.; Portugall, O.; Eperon, G. E.; Wang, J. T. W.; Stergiopoulos, T.; Stranks, S. D.; Snaith, H. J.; Nicholas, R. J. Determination of the Exciton Binding Energy and Effective Masses for Methylammonium and Formamidinium Lead Tri-Halide Perovskite Semiconductors. *Energy Environ. Sci.* **2016**, *9* (3), 962−970.
(47) Li, B.; Long, R.; Xia, Y.; Mi, Q. All-Inorganic Perovskite CsSnBr3 as a Thermally Stable, Free-Carrier Semiconductor. *Angew. Chem., Int. Ed.* **2018**, *57* (40), 13154−13158.
(48) Gallop, N. P.; Selig, O.; Giubertoni, G.; Bakker, H. J.; Rezus, Y. L. A.; Frost, J. M.; Jansen, T. L. C.; Lovrincic, R.; Bakulin, A. A. Rotational Cation Dynamics in Metal Halide Perovskites: Effect on Phonons and Material Properties. *J. Phys. Chem. Lett.* **2018**, *9* (20), 5987−5997.
(49) Mishra, A.; Hope, M. A.; Grätzel, M.; Emsley, L. A Complete Picture of Cation Dynamics in Hybrid Perovskite Materials from Solid-State NMR Spectroscopy. *J. Am. Chem. Soc.* **2023**, *145* (2), 978−990.
(50) Ghosh, D.; Walsh Atkins, P.; Islam, M. S.; Walker, A. B.; Eames, C. Good Vibrations: Locking of Octahedral Tilting in Mixed-Cation Iodide Perovskites for Solar Cells. *ACS Energy Lett.* **2017**, *2* (10), 2424−2429.
(51) Ghosh, D.; Smith, A. R.; Walker, A. B.; Islam, M. S. Mixed A-Cation Perovskites for Solar Cells: Atomic-Scale Insights Into Structural Distortion, Hydrogen Bonding, and Electronic Properties. *Chem. Mater.* **2018**, *30* (15), 5194−5204.
(52) Mayers, M. Z.; Tan, L. Z.; Egger, D. A.; Rappe, A. M.; Reichman, D. R. How Lattice and Charge Fluctuations Control Carrier Dynamics in Halide Perovskites. *Nano Lett.* **2018**, *18* (12), 8041−8046.
(53) Tao, S.; Schmidt, I.; Brocks, G.; Jiang, J.; Tranca, I.; Meerholz, K.; Olthof, S. Absolute Energy Level Positions in Tin- and Lead-Based Halide Perovskites. *Nature Communications 2019 10:1* **2019**, *10* (1), 1−10.
(54) Zhou, G.; Chu, W.; Prezhdo, O. V. Structural Deformation Controls Charge Losses in MAPbI3: Unsupervised Machine Learning of Nonadiabatic Molecular Dynamics. *ACS Energy Lett.* **2020**, *5* (6), 1930−1938.
(55) Liu, D.; Perez, C. M.; Vasenko, A. S.; Prezhdo, O. V. Ag-Bi Charge Redistribution Creates Deep Traps in Defective Cs2AgBiBr6: Machine Learning Analysis of Density Functional Theory. *J. Phys. Chem. Lett.* **2022**, *13* (16), 3645−3651.
(56) Mangan, S. M.; Zhou, G.; Chu, W.; Prezhdo, O. V. Dependence between Structural and Electronic Properties of CsPbI3: Unsupervised Machine Learning of Nonadiabatic Molecular Dynamics. *J. Phys. Chem. Lett.* **2021**, *12* (35), 8672−8678.
(57) Ghosh, D.; Perez, C. M.; Prezhdo, O.; Nie, W.; Tretiak, S.; Neukirch, A. J. Impact of Composition Engineering on Charge Carrier Cooling in Hybrid Perovskites: Computational Insights. *J. Mater. Chem. C Mater.* **2022**, *10* (25), 9563−9572.
(58) Ghosh, D.; Acharya, D.; Pedesseau, L.; Katan, C.; Even, J.; Tretiak, S.; Neukirch, A. J. Charge Carrier Dynamics in Two-Dimensional Hybrid Perovskites: Dion-Jacobson vs. Ruddlesden-Popper Phases. *J. Mater. Chem. A Mater.* **2020**, *8* (42), 22009−22022.
(59) Nayak, P. K.; Ghosh, D. Tuning Charge Carrier Dynamics through Spacer Cation Functionalization in Layered Halide Perovskites: An Ab Initio Quantum Dynamics Study. *J. Mater. Chem. C Mater.* **2023**, *11* (10), 3521−3532.
(60) Slavney, A. H.; Hu, T.; Lindenberg, A. M.; Karunadasa, H. I. A Bismuth-Halide Double Perovskite with Long Carrier Recombination Lifetime for Photovoltaic Applications. *J. Am. Chem. Soc.* **2016**, *138* (7), 2138−2141.
(61) Jöbsis, H. J.; Caselli, V. M.; Askes, S. H. C.; Garnett, E. C.; Savenije, T. J.; Rabouw, F. T.; Hutter, E. M. Recombination and Localization: Unfolding the Pathways behind Conductivity Losses in Cs2AgBiBr6 Thin Films. *Appl. Phys. Lett.* **2021**, *119* (13), 131908.
(62) Hedley, G. J.; Quarti, C.; Harwell, J.; Prezhdo, O. V.; Beljonne, D.; Samuel, I. D. W. Hot-Hole Cooling Controls the Initial Ultrafast Relaxation in Methylammonium Lead Iodide Perovskite. *Scientific Reports 2018 8:1* **2018**, *8* (1), 1−9.
(63) Strandell, D.; Mora Perez, C.; Wu, Y.; Prezhdo, O. V.; Kambhampati, P. Excitonic Quantum Coherence in Light Emission from CsPbBr3Metal-Halide Perovskite Nanocrystals. *Nano Lett.* **2024**, *24* (1), 61−66.
(64) Strandell, D.; Wu, Y.; Mora-Perez, C.; Prezhdo, O.; Kambhampati, P. Breaking the Condon Approximation for Light Emission from Metal Halide Perovskite Nanocrystals. *J. Phys. Chem. Lett.* **2023**, *14* (50), 11281−11285.
(65) Tang, X.; Wen, X.; Yang, F. Ultra-Stable Blue-Emitting Lead-Free Double Perovskite Cs2SnCl6 Nanocrystals Enabled by an Aqueous Synthesis on a Microfluidic Platform. *Nanoscale* **2022**, *14* (47), 17641−17653.
(66) Bhat, A. A.; Farooq, A.; Mearaj, T.; Sheikh, Z. A.; Bajaber, M. A.; Alshomrany, A. S. Bandgap Engineering through Fe Doping in Cs2SnCl6 Perovskite: Photoluminescence Characteristics and Electronic Structure Insights. *Energy Fuels* **2024**, *38*, 5465.
(67) Gong, X.; Voznyy, O.; Jain, A.; Liu, W.; Sabatini, R.; Piontkowski, Z.; Walters, G.; Bappi, G.; Nokhrin, S.; Bushuyev, O.; Yuan, M.; Comin, R.; McCamant, D.; Kelley, S. O.; Sargent, E. H. Electron-Phonon Interaction in Efficient Perovskite Blue Emitters. *Nat. Mater.* **2018**, *17* (6), 550−556.
(68) Gallop, N. P.; Maslennikov, D. R.; Mondal, N.; Goetz, K. P.; Dai, Z.; Schankler, A. M.; Sung, W.; Nihonyanagi, S.; Tahara, T.; Bodnarchuk, M. I.; Kovalenko, M. V.; Vaynzof, Y.; Rappe, A. M.; Bakulin, A. A. Ultrafast Vibrational Control of Organohalide Perovskite Optoelectronic Devices Using Vibrationally Promoted Electronic Resonance. *Nature Materials 2023 23:1* **2024**, *23* (1), 88−94.

https://doi.org/10.1021/acs.chemmater.4c00290
Chem. Mater. 2024, 36, 3875−3885

(69) Gumber, S.; Eniodunmo, O.; Ivanov, S. A.; Kilina, S.; Prezhdo, O. V.; Ghosh, D.; Tretiak, S. Hot Carrier Relaxation Dynamics in Non-Stoichiometric CdSe Quantum Dots: Computational Insights. *J. Mater. Chem. A Mater.* **2023**, *11* (15), 8256−8264.
(70) Chu, W.; Zheng, Q.; Prezhdo, O. V.; Zhao, J.; Saidi, W. A. Low-Frequency Lattice Phonons in Halide Perovskites Explain High Defect Tolerance toward Electron-Hole Recombination. *Sci. Adv.* **2020**, *6* (7), 7453−7467.
(71) Neukirch, A. J.; Abate, I. I.; Zhou, L.; Nie, W.; Tsai, H.; Pedesseau, L.; Even, J.; Crochet, J. J.; Mohite, A. D.; Katan, C.; Tretiak, S. Geometry Distortion and Small Polaron Binding Energy Changes with Ionic Substitution in Halide Perovskites. *J. Phys. Chem. Lett.* **2018**, *9* (24), 7130−7136.
(72) Kresse, G.; Hafner, J. *Ab Initio* Molecular-Dynamics Simulation of the Liquid-Metal-Amorphous-Semiconductor Transition in Germanium. *Phys. Rev. B* **1994**, *49* (20), 14251.
(73) Kresse, G.; Hafner, J. *Ab Initio* Molecular Dynamics for Liquid Metals. *Phys. Rev. B* **1993**, *47* (1), 558.
(74) Kresse, G.; Furthmüller, J. Efficient Iterative Schemes for *Ab Initio* Total-Energy Calculations Using a Plane-Wave Basis Set. *Phys. Rev. B* **1996**, *54* (16), 11169.
(75) Kresse, G.; Joubert, D. From Ultrasoft Pseudopotentials to the Projector Augmented-Wave Method. *Phys. Rev. B* **1999**, *59* (3), 1758.
(76) Perdew, J. P.; Burke, K.; Ernzerhof, M. Generalized Gradient Approximation Made Simple. *Phys. Rev. Lett.* **1996**, *77* (18), 3865.
(77) Grimme, S.; Antony, J.; Ehrlich, S.; Krieg, H. A Consistent and Accurate Ab Initio Parametrization of Density Functional Dispersion Correction (DFT-D) for the 94 Elements H-Pu. *J. Chem. Phys.* **2010**, *132* (15), 154104.
(78) Monkhorst, H. J.; Pack, J. D. Special Points for Brillouin-Zone Integrations. *Phys. Rev. B* **1976**, *13* (12), 5188.
(79) Ganose, A. M.; Jackson, A. J.; Scanlon, D. O. *Sumo: Command-Line Tools for Plotting and Analysis of Periodic Ab Initio Calculations Software • Review • Repository • Archive*; 2018.
(80) Momma, K.; Izumi, F. VESTA 3 for Three-Dimensional Visualization of Crystal, Volumetric and Morphology Data. *J. Appl. Crystallogr.* **2011**, *44* (6), 1272−1276.
(81) Humphrey, W.; Dalke, A.; Schulten, K. VMD: Visual Molecular Dynamics. *J. Mol. Graph* **1996**, *14* (1), 33−38.
(82) Akimov, A. V.; Prezhdo, O. V. The PYXAID Program for Non-Adiabatic Molecular Dynamics in Condensed Matter Systems. *J. Chem. Theory Comput* **2013**, *9* (11), 4959−4972.
(83) Akimov, A. V.; Prezhdo, O. V. Advanced Capabilities of the PYXAID Program: Integration Schemes, Decoherence Effects, Multiexcitonic States, and Field-Matter Interaction. *J. Chem. Theory Comput* **2014**, *10* (2), 789−804.
(84) Kraskov, A.; Stögbauer, H.; Grassberger, P. Estimating Mutual Information. *Phys. Rev. E Stat Phys. Plasmas Fluids Relat Interdiscip Topics* **2004**, *69* (6), 16.

https://doi.org/10.1021/acs.chemmater.4c00290
Chem. Mater. 2024, 36, 3875−3885